Research Article J. Electrochem. Sci. Technol., **2020**, *11(1), 50-59*

PEDOT:PSS Enhanced Electrochemical Capacitive Performance of Graphene-Templated δ-MnO_2

Neriman Sinan[1] and Ece Unur[2]*

[1]*Graduate School of Natural and Applied Sciences, Advanced Technologies-Materials Science and Engineering Program, Bursa Technical University, Yildirim 16310, Bursa, Turkey*

[2]*Department of Energy Systems Engineering, Bursa Technical University, Yildirim 16310, Bursa, Turkey*

ABSTRACT

Birnessite-type manganese dioxide (δ-MnO_2) with hierarchical micro-/mesoporosity was synthesized via sacrificial graphene template approach under mild hydrothermal conditions for the first time. Graphene template was obtained by a surfactant (cetyltrimethylammonium bromide, CTAB) assisted liquid phase exfoliation (LPE) in water. A thin PEDOT:PSS (poly (3,4-ethylene dioxythiophene): poly (styrene sulfonate)) layer was applied to improve electrical conductivity and rate capability of MnO_2. The MnO_2 (535 F g^{-1} at 1 A g^{-1} and 45 F g^{-1} at 10 A g^{-1}) and MnO_2/PEDOT:PSS nanocomposite (550 F g^{-1} at 1 A g^{-1} and 141 F g^{-1} at 10 A g^{-1}) delivered electrochemical performances superior to their previously reported counterparts. An asymmetric supercapacitor, composed of MnO_2/PEDOT:PSS (positive) and Fe_3O_4/Carbon (negative) electrodes, provided a maximum specific energy of 18 Wh kg^{-1} and a maximum specific power of 4.5 kW kg^{-1} (ΔV= 2 V, 1M Na_2SO_4) with 85% capacitance retention after 1000 cycles. The graphene-templated MnO_2/PEDOT:PSS nanocomposite obtained by a simple and green approach promises for future energy storage applications with its remarkable capacitance, rate performance and cycling stability.

Keywords : Graphene, Liquid Exfoliation, MnO_2, PEDOT:PSS, Supercapacitor

Received : 6 March 2019, Accepted : 16 August 2019

1. Introduction

Integration of intermittent renewable energy resources (solar and wind) into grids require utilization of efficient energy storage technologies. Higher specific powers and longer cycle lives of supercapacitors make them particularly appropriate for grid applications as they can buffer short-term power fluctuations [1,2]. However, supercapacitors exhibit significantly lower specific energy than batteries. Thus, low-cost electrode materials with simultaneously high specific power and specific energy must be engineered by scalable methods to exploit the full potential of supercapacitors and to push the technology forward [3,4].

Pseudocapacitive electrode materials (transition metal oxides, conductive polymers) store energy via reversible charge transfer (faradaic) reactions at the electrode surface. They offer great potential to overcome specific energy limitation as they can achieve higher capacitances compared to carbonaceous materials (graphene, activated carbon, CNT, etc.) that store energy statically at the electric double layer (EDL) [4]. Manganese dioxide (MnO_2) was first exploited as a pseudocapacitive material by Lee and Goodenough in 1999 [5]. The intense interest in MnO_2 for supercapacitor applications is driven by its low toxicity, high theoretical capacitance (1370 F g^{-1} over a potential window of 0.8 V, assuming the transfer of one electron per Mn atom) [6], and low cost. MnO_2 exhibits a rich polymorphism as its building [MnO_6] octahedral units form numerous three-dimensional structures with tunnels or interlayers that can facilitate ion intercalation. The birnessite-type manganese dioxide (δ-MnO_2) consists of stacked monolayers (0.7 nm interlayer distance) of edge-shared [MnO_6] octahedra and has the most open structure of all MnO_2 polymorphs [7]. However, low electrical conductivity (10^{-5}-10^{-6} S cm^{-1}) and poor cycling stability hinder elec-

*E-mail address: eceunur@gmail.com

DOI: https://doi.org/10.33961/jecst.2019.03475

trochemical performance of MnO_2 [5]. To overcome these disadvantages, MnO_2 has been incorporated by carbonaceous materials, graphene and its derivatives or conductive polymers [8-11].

Besides being used as a conductive additive, graphene can function as a sacrificial template in synthesis of MnO_2 nanostructures with controlled morphology and improved electrochemical performance. Graphene oxide (GO) [12] and reduced graphene oxide (rGO) [13] were reported to induce the growth of δ-type MnO_2 by *in-situ* replacement of graphene carbons by edge-sharing [MnO_6] octahedra when used as sacrificial templates. However, the synthesis of GO/rGO is a laborious multi-step process which requires the use of harsh chemicals [9]. Moreover, dense oxygen groups and defects on GO and rGO hinder homogeneous distribution of MnO_2 particles and lead to irregular morphologies, whereas π-conjugated defect-free graphene enables efficient templating. Lately, an environmentally benign single-step *liquid-phase exfoliation (LPE)* has become a prominent non-oxidative method in bulk production of defect-free graphene [14,15]. Chen et al. utilized graphene, exfoliated in an organic solvent N-methyl-pyrrolidone, as a sacrificial template in synthesis of MnO_2 nanolamellas and reported a specific capacitance of 206 F g^{-1} [16].

In this work, a defect-free graphene was obtained by a scalable and environmentally benign surfactant-assisted liquid-phase exfoliation (LPE) in water. To our knowledge, this is the first report on the use of water-driven exfoliated graphene as a sacrificial template in synthesis of δ-MnO_2 under hydrothermal conditions. Graphene-templated MnO_2 exhibited a specific capacitance higher than that of its previously reported carbon and conductive polymer composites. PEDOT: PSS coating further enhanced the capacitance and the rate capability of the MnO_2. Asymmetric supercapacitor composed of MnO_2/PEDOT:PSS (positive electrode) and Fe_3O_4/C (negative electrode) promises for future practical applications with its high specific energy (18 Wh kg^{-1}), specific power (4.5 kW kg^{-1}) and cycling stability (85% capacitance retention after 1000 cycles).

2. Experimental

2.1 Preparation of colloidal graphene

The cationic surfactant-stabilized graphene dispersions were prepared by sonicating a mixture of 500 mg of graphite powder (< 20 μm, Sigma Aldrich) and 25 mg of hexadecyl trimethyl ammonium bromide (CTAB, Sigma Aldrich) in deionized (DI) water (50 mL) with a Bandelin Sonopuls HD3200 ultrasonic homogenizer (microtip MS 73, dia. 3 mm). The sonicator was operated at 65% amplitude of 200 W and 20 kHz for 1.5 h in the pulse mode (1-s on, 0.5-s off) in an ice bath. The resulting dispersion was left to sit for ~20 h allowing aggregation to form and then centrifuged (Allegra X-30R, Beckman Coulter, USA) at 2000 rpm for 30 min. The precipitate was discarded and supernate was collected for further use. The yield was recorded as ~0.4 mg ml^{-1}.

2.2 Preparation of exfoliated graphene-induced MnO_2

315 mg potassium permanganate ($KMnO_4$, Kimetsan) was mixed with 30 mL of exfoliated graphene dispersion (~0.4 mg mL^{-1}) and hydrothermally treated for 8 h at 160°C in a stainless steel autoclave. Before drying at 80°C, the sample was washed with ethanol and DI water.

2.3 Preparation of MnO_2/PEDOT:PSS nanocomposite

200 mg of MnO_2 powder was dispersed in 30 mL DI water, then 0.5 mL of PEDOT:PSS solution (solid content: 3.0 - 4.0 wt% in H_2O, Sigma Aldrich) was added into the dispersion and vigorously stirred overnight. The product was washed with ethanol and DI water and dried at 60°C under vacuum.

2.4 Material Characterizations

QUANTA 400F field emission scanning electron microscope (FE-SEM) and JEOL JEM-2100F transmission electron microscope (TEM) were used to investigate structural properties of samples. Before SEM imaging, samples were coated with a thin Au-Pd layer (2-5 nm). EDS (Energy dispersive X-ray spectroscopy) mapping was performed by ZEISS/GeminiSEM 300 with a Bruker X-Flash 100 detector. Rigaku Ultima-IV diffractometer equipped with a CuKα source was used to perform X-Ray diffraction (XRD) studies (scan rate: 0.6° min^{-1}). Raman spectra were recorded with 532 nm laser excitation (Renishaw InVia dispersive Raman microscope). X-ray photoelectron spectroscopy (XPS) analyses were performed on a PHI 5000 VersaProbe instrument with a

monochromatic AlKα source. Samples were evacuated at 200°C for 10 hours and subjected to nitrogen (77 K) gas adsorption-desorption using a Quantachrome Autosorb-6 instrument. Brunauer-Emmett-Teller (BET) method and Density Functional Theory (DFT) were used to determine the specific surface area and pore size distribution, respectively.

2.5 Electrochemical measurements

Active material, polyvinylidene fluoride binder (PVDF, Kynar® HSV 900) and conductive carbon black (Timcal Graphite & Carbon Super P®) were mixed in N-methylpyrrolidone (NMP, Merck) at 80:10:10 weight ratio. Then, this slurry was coated onto a stainless steel foil (MTI) in the form of a 500 µm thick film. After drying overnight at room temperature, the electrodes were further dried under vacuum (60°C, 4 h).

For the three-electrode measurements, a platinum wire and a silver/silver chloride (Ag/AgCl sat. with KCl (aq)) electrodes served as the counter and reference electrodes, respectively. The mass loading of the working electrodes was ~3 mg cm^{-2}. Cyclic voltammetry (CV) and galvanostatic charge-discharge (GCD) tests were realized in 1 M sodium sulphate (Na_2SO_4, Sigma Aldrich) aqueous solution (0 - 1.2 V vs. Ag/AgCl) by using a Gamry potentiostat/galvanostat (Reference 3000). The specific capacitances C_s (F g^{-1}) were calculated with respect to the following equation: $C_s = (I \times \Delta t)/(m \times \Delta V)$ where ΔV (V) is the width of potential (the IR-drop excluded), I (A) is the discharge current, m (g) is the mass of active material and Δt (s) is the discharge time

2.6 Fabrication of asymmetric supercapacitors

To assemble an asymmetric supercapacitor (ASC), a glass fiber separator (Millipore®, thickness: 475 µm) saturated by 1M Na_2SO_4 aqueous electrolyte was sandwiched between the negative Fe_3O_4/Carbon (reported in our previous work [17]) and positive MnO_2 or MnO_2/PEDOT:PSS electrodes. The charge balance ($q^+ = q^-$) was ensured by adjusting the mass ratio of positive/negative electrodes ($q = C_s \times \Delta V \times m$). CV, GCD, and cycle life measurements were performed within a potential range of 0 to 2.0 V. The following equations were used to calculate specific energy E_{cell} (Wh kg^{-1}) and specific power P_{cell} (W kg^{-1}) of the cell: $E_{cell} = (0.5 \times C_{s,cell} \times \Delta V^2)/3.6$ and $P_{cell} = E/t \times 3600$ where $C_{s,cell}$ is the specific capacitance of the cell and t (s) is the discharge time. The Coulombic efficiency was calculated according to: $\eta = (t_d/t_c) \times 100$ where t_c and t_d refer to total charge and discharge times, respectively.

3. Results and Discussion

In liquid phase exfoliation, surfactant molecules lower the surface tension of water to overcome Van der Waals forces between graphene sheets. Moreover, CTAB molecules adsorbed onto the electron-rich graphene sheets create electrostatic repulsions and prevent re-stacking [18]. Fig. 1a demonstrates the digital image of the highly stable surfactant-stabilized graphene dispersion taken one year after its preparation. The TEM image of the dispersion reveals overlapping few-layer graphene (FLG) sheets (Fig. 1b). Complementary *in situ* Raman spectroscopy studies were performed to verify the formation of FLG (Fig. 1c). Low-intensity D band (at

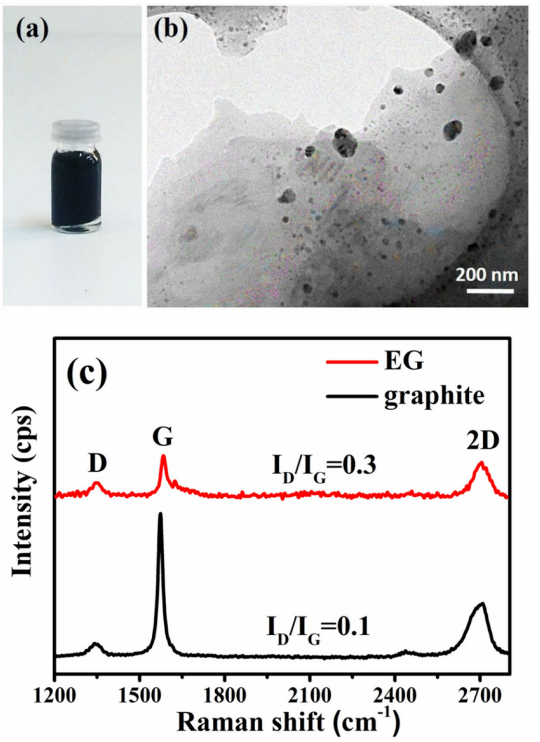

Fig. 1. (a) Digital image of the exfoliated graphene (EG) dispersion (1 year after its preparation), **(b)** TEM image of the EG dispersion, **(c)** Raman spectra of the graphite and the EG (normalized to the G band).

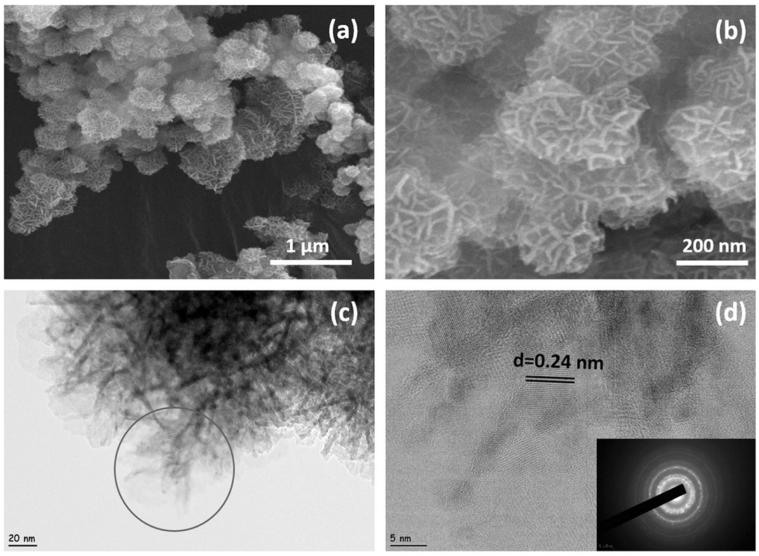

Fig. 2. (a, b) SEM images of MnO_2 and (c, d) TEM images and the selected area diffraction pattern (SAED) of MnO_2.

~1350 cm^{-1}) observed in both graphite and graphene spectra can be ascribed to A_{1g} breathing mode of hexagonal rings and result from the basal plane or edge defects. The G band emerges from first-order scattering of E_{2g} phonons that involves in-plane bond-stretchings of sp^2 carbons. The intensity of the G band decreases and shifts to a higher frequency (from 1573 to 1585 cm^{-1}) going from graphite to exfoliated graphene (EG), as less sp^2 carbons are detected with decreasing number of graphene layers [19]. The number of graphene layers are reported to be less than 5 when the intensity ratio of 2D to G band (I_{2D}/I_G) is equal to or greater than one [20]. FWHM (full-width at half-maximum) of the 2D band is reported to be less than 30 cm^{-1} for single-layer graphene and increase to 65-70 cm^{-1} for FLG [19]. EG showed 2D band characteristics typical of few-layer graphene with a FWHM of 70 cm^{-1} (from Lorentzian fit) and a I_{2D}/I_G value of 0.8 [19,21]. Liquid phase exfoliation method utilized here allowed production of graphene sheets with a lower number of defects (defect ratio=I_D/I_G=0.3) compared to chemically reduced graphene oxides (rGO) reported in the literature (I_D/I_G= 1.2 - 1.5) [22,23].

Exfoliated graphene (EG) sheets were used as a sacrificial template to induce the growth of birnessite-type MnO_2 nanoparticles under hydrothermal conditions. The C atoms of EG sheets reduce $KMnO_4$ (Mn^{+7}) to Mn^{+4} and initiate the nucleation of MnO_2 on the graphene surface: $4KMnO_4 + 3C + H_2O \rightarrow 4MnO_2 + K_2CO_3 + 2KHCO_3$. The $KMnO_4$-limited hydrothermal reaction proceeds faster and dominates the growth of the MnO_2 nanosheets: $4KMnO_4 + 2H_2O \rightarrow 4MnO_2 + 4KOH + 3O_2$ [8,24]. The graphene-templated growth of MnO_2 nanosheets proceeds along the ab plane and leads to formation of layered birnessite-type MnO_2 [8]. As revealed by SEM images (Fig. 2a, b), MnO_2 nanosheets with a thickness of 10 nm assemble into flower-like nanospheres (200-300 nm in diameter) forming a hierarchical morphology which promotes efficient electrode-electrolyte interactions and fast transport of ions. TEM images (Fig. 2c, d) reveal lattice spacing of 0.24 nm corresponding to (101) plane of birnessite-type MnO_2. Lattice fringes in different orientations indicate the polycrystalline nature of MnO_2 in line with the SAED pattern.

The XPS survey spectrum (Fig. 3a) confirms the existence of Mn and O elements in the MnO_2 sample. The trace K 2p and C 1s peaks in the spectrum result from stabilizing interlayer K^+ cations and residual graphene template, respectively. The spin-induced energy separation between Mn $2p_{1/2}$ and Mn $2p_{3/2}$ peaks was calculated as 11.7 eV, confirming the oxidation state of +4 for Mn (Fig. 3a- inset) [25,26]. The three oxygen peaks detected in the O 1s spectrum (Fig. 3b) can be assigned to the lattice oxygens in [MnO_6] unit cells (527.4 eV), the Mn-OH (528.9 eV), and H-O-H groups (529.9 eV) [27].

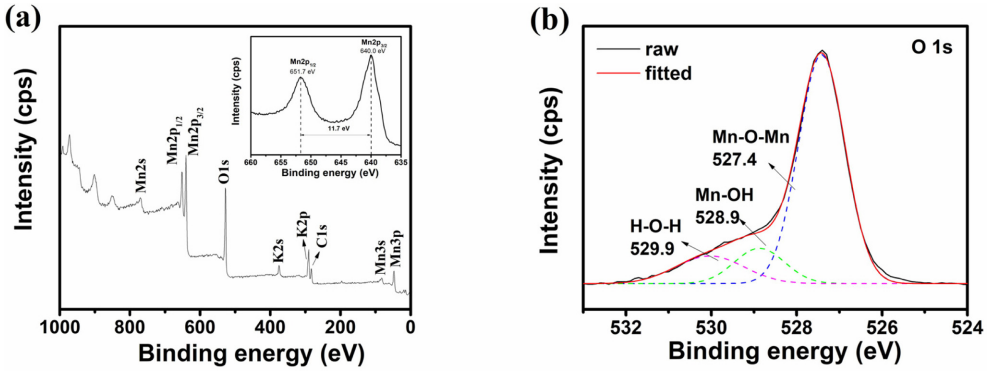

Fig. 3. XPS spectra of MnO_2: (a) survey spectrum with an inset showing Mn 2p region and (b) O 1s region.

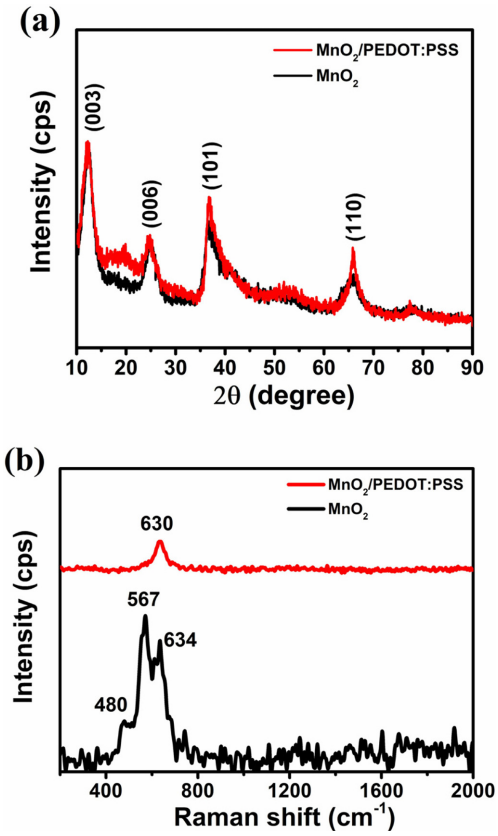

Fig. 4. (a) X-ray diffractograms and (b) Raman spectra of MnO_2 and MnO_2/PEDOT:PSS.

Graphene-templated MnO_2 nanostructures were coated with a thin conductive PEDOT:PSS layer to enhance capacitive performance. The four XRD peaks at 12.3°, 24.8°, 36.6° and 65.5° observed both for the MnO_2 and MnO_2/PEDOT:PSS samples (Fig. 4a) can be indexed to hexagonal birnessite-type MnO_2 [28]. The 7.170 Å interlayer space (d_{003}) indicates the birnessite structure consisting of stacked monolayers of edge-shared [MnO_6] octahedra intercalated by K^+ cations and H_2O molecules. The additional broad peak at 19° with a d-spacing of 4.62 Å observed in MnO_2/PEDOT:PSS pattern is attributed to π-stacked PEDOT:PSS [29]. In the Raman spectrum of MnO_2 (Fig. 4b), three characteristic Mn–O lattice vibrations of birnessite-type MnO_2 were observed at 480, 567, and 634 cm^{-1} [30]. In the MnO_2/PEDOT:PSS sample, Mn–O lattice vibrations merged into one broad peak at 630 cm^{-1} as a result of thin PEDOT:PSS coating.

Specific surface area and porosity of the samples were investigated by Nitrogen (77 K) gas-sorption measurements (Fig. 5). According to IUPAC classification [31], both samples show Type IV isotherm with an H3 type hysteresis indicating mesoporous structure (Fig. 5a). The higher amount of adsorption at low relative pressures ($P/P^o<0.1$) observed for MnO_2/PEDOT:PSS indicates the presence of micropores and the larger width of the hysteresis indicates higher volume of mesopores. Both samples display narrow pore size distribution with peak maximums located at 5.3 nm while MnO_2/PEDOT:PSS has an additional low-intensity peak at 1.2 nm (Fig. 5b). PEDOT:PSS coating increases the BET specific surface area from 78.3 m^2g^{-1} to 200.9 m^2g^{-1} and the corresponding pore volume from 0.09 cm^3g^{-1} to 0.24 cm^3g^{-1}. Hierarchically porous MnO_2/PEDOT:PSS promises higher capacitance as micropores (< 2 nm) provide additional surface for elec-

trode-electrolyte interactions and high rate capability as mesopores (2-50 nm) provide fast ion transport during charge-discharge.

3.1 Electrochemical studies

Energy storage capabilities of the MnO_2 and MnO_2/PEDOT:PSS samples were investigated by cyclic vol-

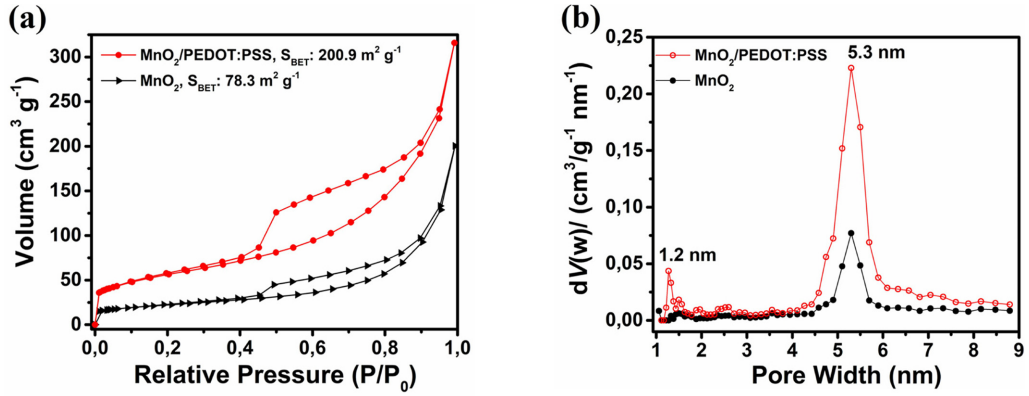

Fig. 5. (a) N_2 gas-sorption isotherms and (b) pore size distributions of MnO_2 and MnO_2/PEDOT:PSS.

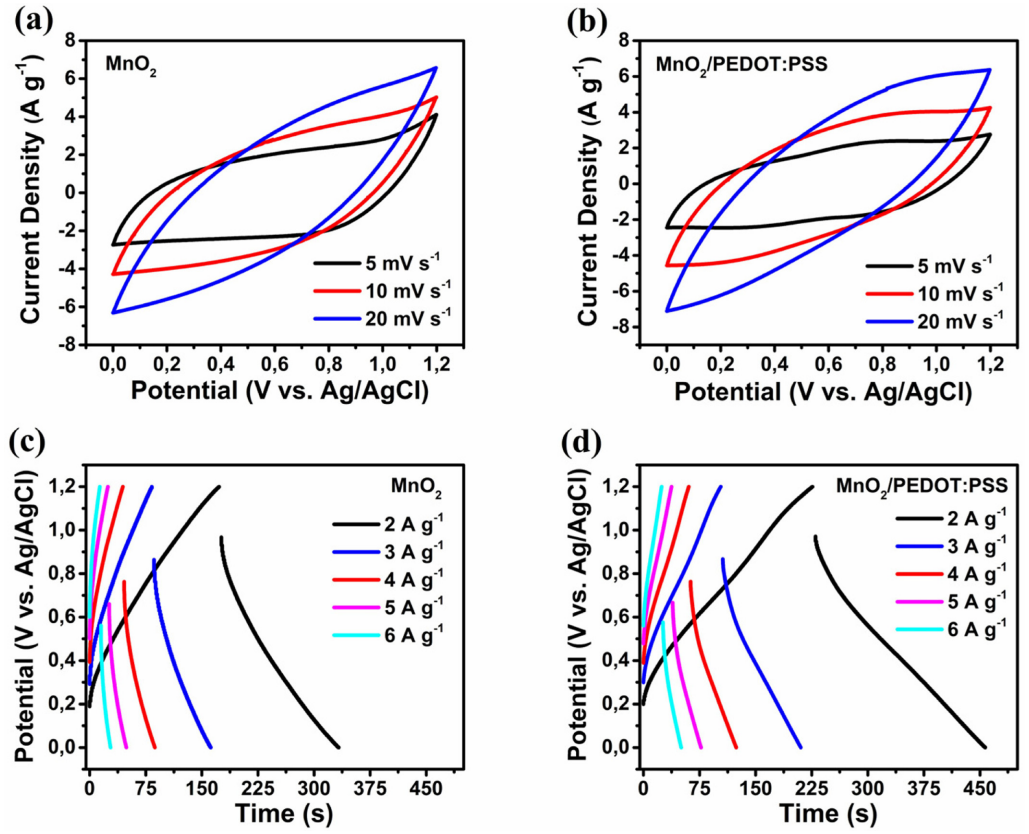

Fig. 6. Cyclic voltammetry (a, b) and charge-discharge (c, d) curves of MnO_2 and MnO_2/PEDOT:PSS at different rates (electrolyte: 1M Na_2SO_4).

tammetry (CV) and galvanostatic charge-discharge (GCD) studies in 1M Na_2SO_4 aqueous electrolyte (0 - 1.2 V vs. Ag/AgCl). Slightly larger CV areas (Fig. 6a, b) and longer discharge times (Fig. 6c, d) observed for MnO_2/PEDOT:PSS indicate higher capacitance compared to MnO_2. Part of this capacitance results from the surface redox reactions between MnO_2 and alkali metal cations (Na^+ in this case) or protons (H^+): $MnO_2 + xNa^+ + yH^+ + (x + y)\ e^- \leftrightarrow MnOONa_xH_y$ [32]. Highly conjugated PEDOT:PSS with high electron mobility improves surface conductivity while PEDOT redox couple aids in overall pseudocapacitance: $PEDOT^+.\ PSS^- + xNa^+ + yH^+ + (x+y)\ e^- \leftrightarrow PEDOT^0.\ PSS^-.\ Na_xH_y$ [33]. The deviation of voltammograms from the standard rectangular shape and the initial voltage (IR) drops at discharge result from diffusion limitations of surface redox reactions.

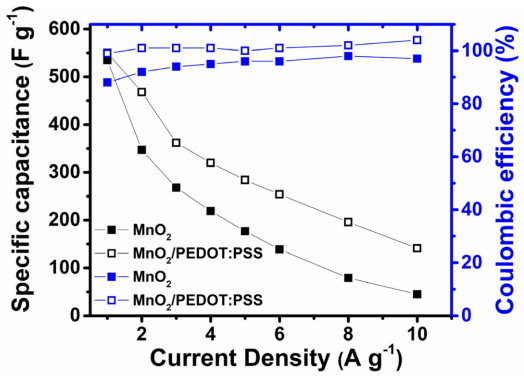

Fig. 7. Rate capabilities of MnO_2 and MnO_2/PEDOT:PSS.

The specific capacitances of the samples are calculated at different current rates (1 to 10 A g^{-1}) and plotted in Fig. 7. Both MnO_2 and MnO_2/PEDOT:PSS provide high specific capacitances at 1 A g^{-1} (535 and 550 F g^{-1}, respectively). PEDOT:PSS polymer coating increases the conductivity and thus coulombic efficiency of MnO_2 from 88% to 99% at 1 A g^{-1}. Higher rate capability of MnO_2/PEDOT:PSS compared to MnO_2 (141 vs. 45 F g^{-1} at 10 A g^{-1}) results from higher volume of mesopores which enable fast

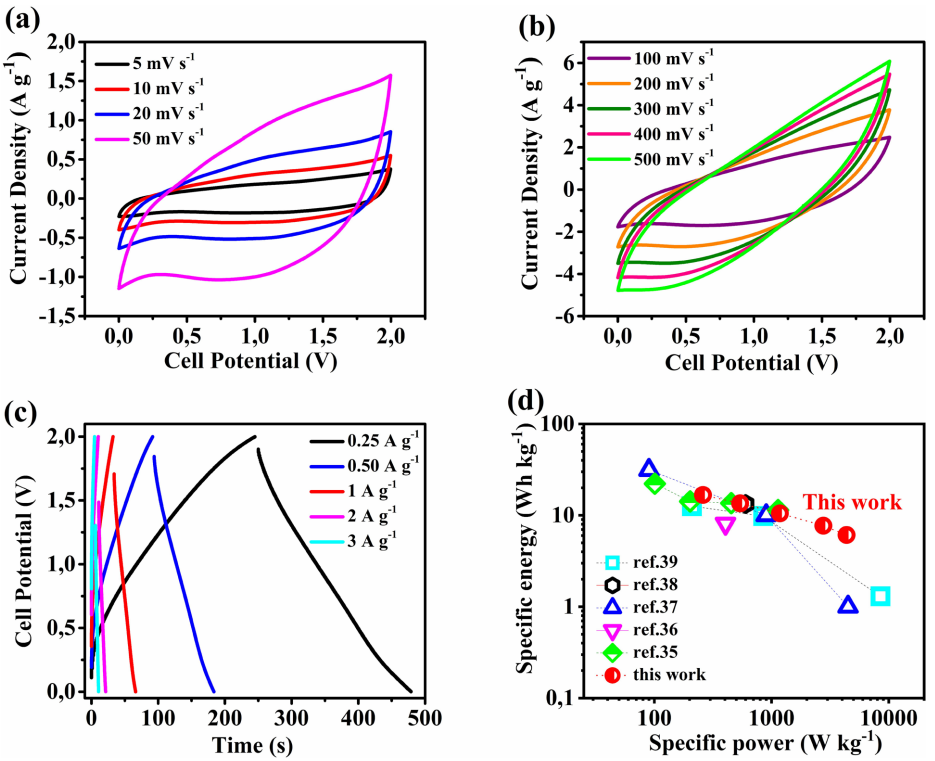

Fig. 8. Electrochemical performance of the Fe_3O_4/C//MnO_2/PEDOT:PSS asymmetric supercapacitor (ΔV= 2 V in 1M $Na_2SO_{4\ (aq)}$): (a, b) CV and (c) GCD curves at different rates, (d) Ragone plot of the device in comparison with MnO_2-based asymmetric supercapacitors reported in the literature.

and easy transport of charge carriers. MnO_2 and MnO_2/PEDOT:PSS samples prepared in this work delivered superior capacitances and rate capabilities compared to previously reported graphene templated MnO_2, MnO_2/rGO and MnO_2/rGO/conductive polymer nanocomposites prepared by harsh chemicals and laborious methods [8-11,13,16,34].

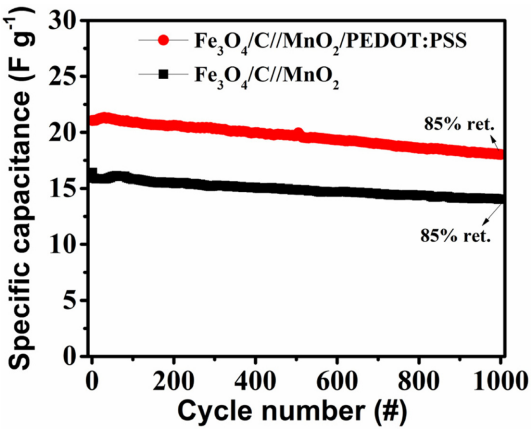

Fig. 9. Cycling stability of asymmetric devices at 1 A g^{-1}.

3.2 Asymmetric Supercapacitors

Asymmetric supercapacitors (ASCs) were assembled with Fe_3O_4/Carbon nanocomposite negative electrode against MnO_2 or MnO_2/PEDOT:PSS positive electrodes. The CV and GCD curves of the devices are recorded in a 1M Na_2SO_4 aqueous electrolyte (ΔV= 2 V). The Fe_3O_4/C//MnO_2/PEDOT:PSS device delivered higher capacitive performance at 1 A g^{-1} charge-discharge rate (C_s = 21 F g^{-1}, E = 12 Wh kg^{-1}, and P = 1.2 kW kg^{-1}) compared to the Fe_3O_4/C// MnO_2 device (C_s = 16 F g^{-1}, E = 9 Wh kg^{-1}, and P = 1.1 kW kg^{-1}). As shown in Fig. 8 the Fe_3O_4/C// MnO_2/PEDOT:PSS device exhibits a maximum specific energy of 18 Wh kg^{-1} (0.25 A g^{-1}) and a maximum specific power of 4.5 kW kg^{-1} (3 A g^{-1}). The Ragone plot (Fig. 8d) compares the performance of MnO_2/PEDOT:PSS device obtained in this work to previously reported MnO_2-based asymmetric supercapacitors and proves better rate capability of the

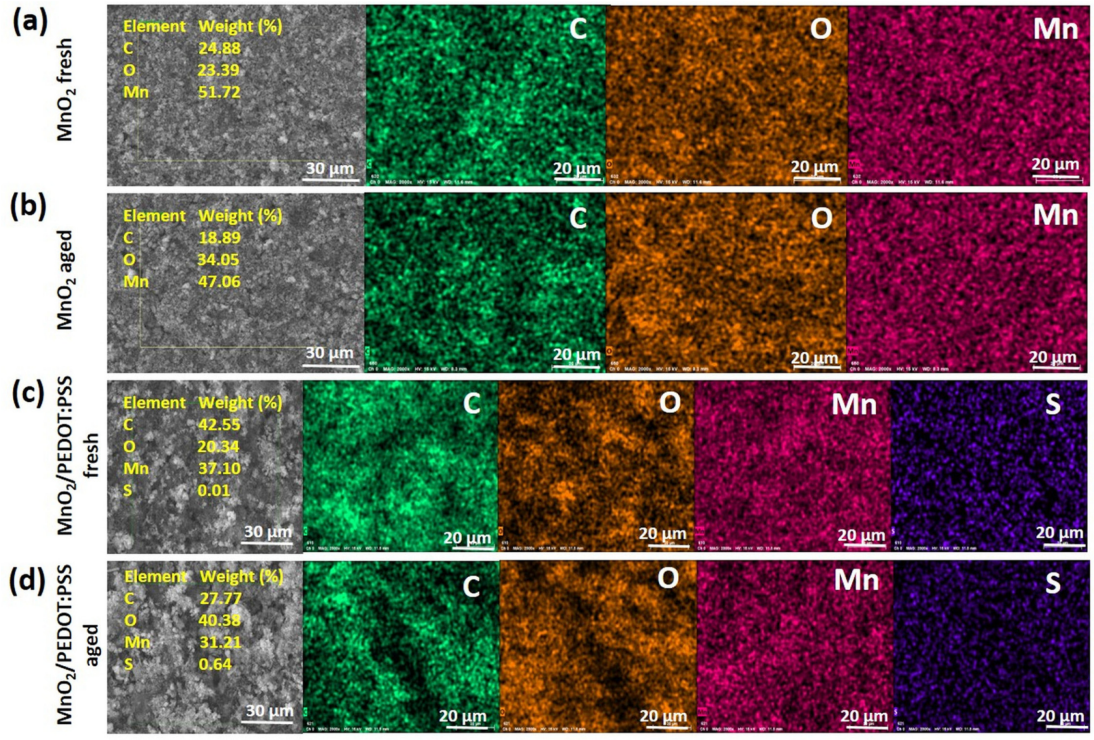

Fig. 10. Elemental mapping of (a, b) MnO_2 and (c, d) MnO_2/PEDOT:PSS electrodes before and after 1000 cycles at 1 A g^{-1} in asymmetric devices.

device [35-39].

The Fe_3O_4/C//MnO_2 and Fe_3O_4/C//MnO_2/PEDOT:PSS asymmetric supercapacitors both remain chemically and structurally intact over the span of 1000 charge-discharge cycles at 1 A g^{-1} and retain 85% of their initial capacitances (Fig. 9). SEM-EDS mappings of MnO_2 and MnO_2/PEDOT:PSS electrodes reveal only 5% active material loss (Mn) after 1000 cycles (Fig. 10) and prove that the open network of MnO_2 enabled by graphene templating prevents microstructural degradation upon continuous charge-discharge.

4. Conclusions

In summary, a simple approach has been demonstrated for producing a high performance nanocomposite electrode consisting of exfoliated graphene-induced δ-MnO_2 and PEDOT:PSS (MnO_2/PEDOT:PSS). A few-layer graphene was produced by a safe and scalable liquid-phase exfoliation (LPE) method and used as a sacrificial template for hydrothermal synthesis of birnessite-type hierarchical manganese oxide (δ-MnO_2). Graphene templating delivered a chemically and structurally intact MnO_2 with a high capacitance and electrochemical cycling stability. Conductive PEDOT:PSS coating further improved the capacitance and rate capability. High performance MnO_2/PEDOT:PSS composite electrode obtained by scalable and environmentally friendly methods promises for future energy storage applications.

Acknowledgement

This work was financially supported by Research Fund of the Bursa Technical University (Project Number: 2016-01-023) and part of the material characterizations were conducted at the Middle East Technical University Central Laboratory and the Bursa Technical University Central Research Laboratory.

References

[1] P. Simon, T. Brousse, and F. Favier, Supercapacitors Based on Carbon or Pseudocapacitive Materials, Vol. 3, Wiley-ISTE, **2017**.
[2] A. Vlad and A. Balducci, *Nat. Mater.*, **2017**, *16(2)*, 161-162.
[3] J. Liu, J. Wang, C. Xu, H. Jiang, C. Li, L. Zhang, J. Lin, and Z.X. Shen, *Adv. Sci.*, **2018**, *5(1)*, 1700322.
[4] P. Simon and Y. Gogotsi, *Nat. Mater.*, **2008**, *7(11)*, 845-854.
[5] H.Y. Lee and J.B. Goodenough, *J. Solid State Chem.*, **1999**, *144(1)*, 220-223.
[6] M. Toupin, T. Brousse, and D. Bélanger, *Chem. Mater.*, **2004**, *16(16)*, 3184-3190.
[7] S. Devaraj and N. Munichandraiah, *J. Phys. Chem. C*, **2008**, *112(11)*, 4406-4417.
[8] Y. Liu, D. Yan, R. Zhuo, S. Li, Z. Wu, J. Wang, P. Ren, P. Yan, and Z. Geng, *J. Power Sources*, **2013**, *242*, 78-85.
[9] D. Yan, Y. Li, Y. Liu, R. Zhuo, B. Geng, Z. Wu, J. Wang, P. Ren, and P. Yan, *Electrochim. Acta*, **2015**, *169*, 317-325.
[10] W. Chen, X. Tao, Y. Li, H. Wang, D. Wei, and C. Ban, *J. Mater. Sci. Mater. Electron.*, **2016**, *27(7)*, 6816-6822.
[11] H. Zhou, Z. Yan, X. Yang, J. Lv, L. Kang, and Z.H. Liu, *Mater. Chem. Phys.*, **2016**, *177*, 40-47.
[12] G. Zhao, J. Li, L. Jiang, H. Dong, X. Wang, and W. Hu, *Chem. Sci.*, **2012**, *3(2)*, 433-437.
[13] Z. Li, J. Wang, Z. Wang, H. Ran, Y. Li, X. Han, and S. Yang, *New J. Chem.*, **2012**, *36(7)*, 1490-1495.
[14] R. Raccichini, A. Varzi, S. Passerini, and B. Scrosati, *Nat. Mater.*, **2015**, *14(3)*, 271-279.
[15] Y.L. Zhong, Z. Tian, G.P. Simon, and D. Li, *Mater. Today*, **2015**, *18(2)*, 73-78.
[16] S. Chen, J. Zhu, and X. Wang, *ACS Nano*, **2010**, *4(10)*, 6212-6218.
[17] N. Sinan and E. Unur, *Mater. Chem. Phys.*, **2016**, *183*, 571-579.
[18] M. Cai, D. Thorpe, D.H. Adamson, and H.C. Schniepp, *J. Mater. Chem.*, **2012**, *22(48)*, 24992-25002.
[19] D. Graf, F. Molitor, K. Ensslin, C. Stampfer, A. Jungen, C. Hierold, and L. Wirtz, *Solid State Commun.*, **2007**, *143(1-2)*, 44-46.
[20] A. Gupta, G. Chen, P. Joshi, S. Tadigadapa, and P.C. Eklund, *Nano Lett.*, **2006**, *6(12)*, 2667-2673.
[21] K.B. Ricardo, A. Sendecki, and H. Liu, *Chem. Commun.*, **2014**, *50(21)*, 2751-2754.
[22] M. Cao, N. Wang, L. Wang, Y. Zhang, Y. Chen, Z. Xie, Z. Li, E. Pambou, R. Li, C. Chen, F. Pan, H. Xu, J. Penny, J.R.P. Webster, and J.R. Lu, *J. Mater. Chem. B*, **2016**, *4(1)*, 152-161.
[23] M. Lotya, P.J. King, U. Khan, S. De, and J.N. Coleman, *ACS Nano*, **2010**, *4(6)*, 3155-3162.
[24] X. Jin, W. Zhou, S. Zhang, and G.Z. Chen, *Small*, **2007**, *3(9)*, 1513-1517.
[25] J. Shang, B. Xie, Y. Li, X. Wei, N. Du, H. Li, W. Hou, and R. Zhang, *ACS Nano*, **2016**, *10(6)*, 5916-5921.
[26] H. Su, P. Zhu, L. Zhang, F. Zhou, G. Li, T. Li, Q. Wang, R. Sun, and C. Wong, *J. Electroanal. Chem.*, **2017**, *786*, 28-34.
[27] D. Yan, P. Yan, S. Cheng, J. Chen, R. Zhuo, J. Feng, and G. Zhang, *Cryst. Growth Des.*, **2009**, *9(1)*, 218-222.
[28] H. Chen, C.-K. Hsieh, Y. Yang, X.Y. Liu, C.-H. Lin, C.-H. Tsai, Z.Q. Wen, F. Dong, and Y.X. Zhang, *ChemElectroChem*, **2017**, *4(9)*, 2414-2422.

[29] X. Zhang, D. Chang, J. Liu, and Y. Luo, *J. Mater. Chem.*, **2010**, *20(24)*, 5080-5085.
[30] C. Julien, M. Massot, R. Baddour-Hadjean, S. Franger, S. Bach, and J.P. Pereira-Ramos, *Solid State Ionics*, **2003**, *159(3-4)*, 345-356.
[31] K.S.W. Sing, *Pure Appl. Chem.*, **1985**, *57(4)*, 603-619.
[32] D. Hou, H. Tao, X. Zhu, and M. Li, *Appl. Surf. Sci.*, **2017**, *419*, 580-585.
[33] J. Kawahara, P.A. Ersman, I. Engquist, and M. Berggren, *Org. Electron.*, **2012**, *13(3)*, 469-474.
[34] B. Mendoza-Sánchez, J. Coelho, A. Pokle, and V. Nicolosi, *Electrochim. Acta*, **2015**, *174*, 696-705.
[35] S. Shivakumara and N. Munichandraiah, *Solid State Commun.*, **2017**, *260*, 34-39.
[36] T. Cottineau, M. Toupin, T. Delahaye, T. Brousse, and D. Bélanger, *Appl. Phys. A*, **2006**, *82(4)*, 599-606.
[37] P. Tang, L. Han, and L. Zhang, *ACS Appl. Mater. Interfaces*, **2014**, *6(13)*, 10506-10515.
[38] L. Li, Z.A. Hu, N. An, Y.Y. Yang, Z.M. Li, and H.Y. Wu, *J. Phys. Chem. C*, **2014**, *118(40)*, 22865-22872.
[39] J. Duay, E. Gillette, R. Liu, and S.B. Lee, *Phys. Chem. Chem. Phys.*, **2012**, *14(10)*, 3329-3337.